





# Shear banding instability in multicomponent metallic glasses: Interplay of composition and short-range order

Kamran Karimi <sup>1,\*</sup>, Amin Esfandiarpour <sup>1</sup>, René Alvarez-Donado <sup>1</sup>, Mikko J. Alava,<sup>1,2</sup> and Stefanos Papanikolaou <sup>1</sup>

<sup>1</sup>*NOMATEN Centre of Excellence, National Center for Nuclear Research, ul. A. Sotana 7, 05-400 Swierk/Otrock, Poland*

<sup>2</sup>*Aalto University, Department of Applied Physics, PO Box 11000, 00076 Aalto, Espoo, Finland*



(Received 24 October 2021; revised 4 February 2022; accepted 17 March 2022; published 28 March 2022)

The shear-banding instability in quasistatically driven bulk metallic glasses emerges from collective dynamics, mediated by shear transformation zones and associated nonlocal elastic interactions. It is also phenomenologically known that sharp structural features of shear bands are typically correlated to the sharpness of the plastic yielding transition, being predominant in commonly studied alloys composed of multiple different elements, that have very different atomic radii. However, in the opposite limit where elements' radii are relatively similar, plastic yielding of bulk metallic glasses is highly dependent on compositional and ordering features. In particular, a known mechanism at play involves the formation of short-range order dominated by icosahedra-based clusters. Here, we report on atomistic simulations of multicomponent metallic glasses with different chemical compositions showing that the degree of strain localization is largely controlled by the interplay between composition-driven icosahedra-ordering and collectively-driven shear transformation zones. By altering compositions, strain localization ranges from diffuse homogenized patterns to singular crack-like features. We quantify the dynamical yielding transition by measuring the atoms' susceptibility to plastic rearrangements, strongly correlated to the local atomic structure. We find that the abundance of short-range ordering of icosahedra within rearranging zones increases glassy materials' capacity to delocalize strain. This could be understood on the basis of structural heterogeneities that are enhanced by the presence of local order. The kind of plastic yielding can be often qualitatively inferred by the commonly used compositional descriptor that characterizes element associations, the misfit parameter  $\delta_a$ , and also by uncommon ones, such as shear-band width and shear-band dynamics' correlation parameters.

DOI: [10.1103/PhysRevB.105.094117](https://doi.org/10.1103/PhysRevB.105.094117)

## I. INTRODUCTION

Failure in sheared metallic glasses (below the glass transition temperature  $T_g$ ) generically occurs via localization of intense, irrecoverable deformation beyond their elastic limit, commonly termed as shear bands [1]. These system-spanning strain features have typically narrow linear (in two dimensions) or planar (in three dimensions) topology along which most of plastic deformation accumulates, while the bulk of the material remains essentially elastically deformed. The underlying microstructural, dynamical mechanism that leads to shear-band nucleation and propagation in glassy metals has been known to follow a generally accepted picture in that the bulk plastic response emerges from *collective* dynamics characterized by shear transformation zones (STZs) [2–5]. Nevertheless, in realistic systems, such as metal alloys, this picture has been thought to be valid in the so-called large-atomic disparity limit, characterized by the misfit coefficient  $\delta_a$  [6], with  $\delta_a > 0.06$  being the *good-glass-forming* limit where the atomic radii of compositional elements are considered to be very different [7]. In this limit, local atomic displacements emerge spatially disordered, and under shear, they resemble the displacements seen in a wider range of soft

glassy solids (i.e., jammed granular media, colloidal glasses, glassy polymers, or foams) within the context of plastic yielding transitions [8–11]. Nonetheless, there is a way to generate a glassy environment in the opposite limit of  $\delta_a \rightarrow 0$  but maintaining a larger number of elements, as in medium/high entropy metallic glasses (see [12] and references therein). In this multicomponent limit, the disorder in atomic displacements emerges as well, but the origin is in the “color” of the atoms (see Fig. 1), meaning the complexity of enthalpic interactions, as opposed to their size. In this limit, the behavior under shear has been a challenging concept that remains unexplored. In this paper, we focus on several multicomponent alloys that have been considered in the literature as medium- and high-entropy alloys [7,13,14], and we compare for their mechanical properties in their corresponding glassy state, which we achieve by fast cooling [15]. In an effort to understand which element/compositional and microstructural features signify the quality of the emergent glass under fast cooling rates, we investigate the correlation between shear-band microstructures with the average stress-strain behavior, and then associate them to the compositional structure. We find that plastic rearrangements strongly correlate to the local atomic structure and the abundance of short-range ordering of icosahedra within rearranging zones increases glassy materials' capacity to delocalize strain. The misfit parameter  $\delta_a$  is correlated to the overall compositional trend, but also

\*Corresponding author: kamran.karimi@ncbj.gov.pl

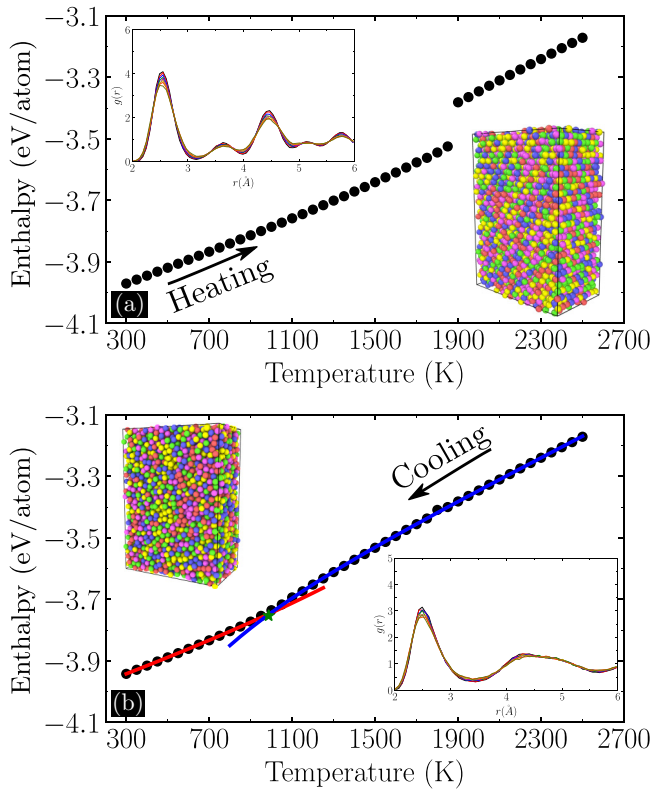


FIG. 1. Evolution of the per-atom enthalpy with temperature for CoNiCrFeMn upon (a) melting (b) quenching at  $\dot{T} = 0.1$  K/ps. The insets show snapshots of atoms and associated radial distribution functions  $g(r)$  at (a)  $T < T_m$  (b)  $T < T_g$ . Here  $T_m \simeq 1900$  K denotes the melting temperature corresponding to the enthalpy jump in (a). The intersection of the nonlinear fits within the solid and liquid phases [32] yields an estimate for the glass transition temperature  $T_g \simeq 1000$  K in (b).

microstructural parameters, such as the emergent shear-band width and shear-band dynamics' correlation, as well as a bulk order parameter tied to the sharpness of plastic yielding transition.

It is currently clear that almost every basic aspect of bulk metallic glasses deformation and failure (e.g., plasticity, shear localization, preparation dependence, strain rate sensitivity, and thermal effects) have been thoroughly understood based on the STZ mechanism [16–18]. Moreover, the general picture concerning the role of STZs in deforming glassy alloys has been further validated universally across. This is remarkable given the inherent disparity of scales, microscopic interactions, and relaxation mechanisms involved. Due to structural and/or mechanical heterogeneity, the coalescence of atomic-scale STZs typically occurs in a highly intermittent and scattered manner both in time and space. On approach to failure, STZ clusters restructure themselves over larger scales leading to the formation of coexisting macroscopic bands with a significant contribution to ductility and plastic flow [19]. On the other hand, certain (aged) glasses that lack this heterogeneity element [20] (or associated lengths don't exceed interatomic scales) tend to localize strain within a single dominant band before the shear banding instability results in a catastrophic brittle-type failure [21].

Several studies highlighted the role of microstructural inhomogeneities in controlling the observed brittle-to-ductile transition. In Refs. [22–24], heterogeneities were mainly attributed to shear-induced crystallization introducing local hardening effects that hinder a dominant band propagation and, in turn, favor nucleation of multiple spontaneous shearing bands. Similar properties were ascribed to quasicrystal-like phases with short range order (SRO) featuring solid-like properties [21,25–27] and, therefore, a strong tendency to tune the extent of strain localization [28–30]. SROs are indeed mediated by the formation of ordered icosahedral clusters as the most (energetically) favored atomic configuration in a quenched metallic glass, which are also greatly responsible for a number of glassy properties such as the dynamical slow down in the super-cooled regime, aging, and dynamic heterogeneity [31]. We note that SROs serve as “infertile” sites for the nucleation of STZs in that the latter are typically loosely-packed soft disordered arrangements that weaken local strength and enhance shear banding instabilities.

The above big picture, however, fails to provide specific details on the precise nature of SRO-induced inhomogeneities and clear description as to how structural heterogeneities evolve at atomic scales and control the shear banding dynamics on macroscopic levels. In this framework, our study aims to establish robust microstructural origins associated with varying degrees of shear localization in driven glassy alloys. Our approach will be based on two (qualitative) themes relevant to the nature of the plastic yielding transition and *quality* of metallic glasses: (i) a “good” glass with a high ability to form localized deformation patterns (ii) a “bad” glass with a tendency to delocalize strain. This might differ from the conventional notion based on the glass forming ability [33] in that good glass formers (typically with notable  $\delta_a$ ) do not necessarily deform well, according to our classification scheme. We will address a fundamental question in the field of metallic glass deformation and failure as to how strain localization may be suppressed by tuning the glassy microstructure within the structure-property paradigm. In the context of the present paper, the above question is reformulated as to how structural heterogeneities may play a role in terms of fine-scale ordering features and how the latter may depend on the glasses chemical compositions. We show that the degree of such correlations controls structural heterogeneities within the glass, and therefore, its capacity to avoid shear band formation.

Our focus will be on certain types of local order, which are purely structural in nature and strongly correlate with (i) dynamics of individual atoms and (ii) bulk stress response in good and bad glasses. The structural metrics used in this study include the density of local icosahedral clusters as well as the radial distribution function of individual atoms. The dynamical property is based on nonaffine displacements, which should entail the atoms propensity to undergo localized rearrangements. We also measure the spontaneous rate of stress release as a relevant mechanical property that helps discern a good glass from a bad one. Using a numerical framework, our paper addresses the intimate structure-dynamics-property relationship by probing the local atoms environment, morphology of nucleated shear bands, and macroscopic stress relaxation and seek for potential

correlations with the composition-based misfit parameter in sheared metallic glasses. The outcomes of our correlation analysis should describe the nature of the plastic yielding transition based upon relevant elemental/microstructural indicators with important implications in terms of materials tailoring to achieve desired mechanical properties.

The organization of the paper is as follows. In Sec. II, the numerical setup, glass preparation, driving protocol, and relevant simulation details are discussed. Section III presents the mechanical response corresponding to several simulated metallic glasses that, depending on chemical compositions, may nucleate diffuse or localized strain patterns. In Sec. IV, we probe the structure-dynamics-property relationship through several structural and dynamical metrics. Sections V and VI present discussions and conclusions, respectively.

## II. SIMULATIONS AND PROTOCOLS

Molecular dynamics simulations were carried out in LAMMPS [34] by implementing atomistic systems of size  $N = 50\,688$  within periodic cubic boxes with  $80 \leq L \leq 90$  Å in a simple-shear loading geometry. The model metallic glasses included in this study are FeNi, CoNiFe, CoNiCrFe, CoCrFeMn, CoNiCrFeMn, and  $\text{Co}_5\text{Cr}_2\text{Fe}_{40}\text{Mn}_{27}\text{Ni}_{26}$ . The interatomic forces were derived from the modified embedded atom method (MEAM) potential with the input parameters associated with the principle elements obtained from [35]. The glassy samples were prepared based on the melt-and-quench protocol illustrated in Fig. 1 plotting the enthalpy of CoNiCrFeMn as a function of temperature. In this context, a crystalline structure was initially heated up to a high temperature (3000 K) above the melting temperature  $T > T_m$ , as in Fig. 1(a), before it was cooled down to the room temperature (300 K) below  $T_g$  at the quench rate of  $\dot{T} = 0.1$  K/ps, as in Fig. 1(b). We allowed for further relaxation upon quenching for order 10 ps to ensure as-quenched glasses are fully equilibrated prior to shearing. The ambient pressure  $P_0$  was set to zero at all times. We also set the discretization time to  $\Delta t = 0.001$  ps. The NPT ensembles were implemented via a Nose-Hoover thermostat and barostat with relaxation time scales  $\tau_d^{\text{therm}} = 0.2$  ps and  $\tau_d^{\text{bar}} = 2.5$  ps. Prior to shearing, the bulk stress tensor  $\sigma_{\alpha\beta} \simeq -P_0 \delta_{\alpha\beta}$  has a nearly hydrostatic form. A strain-controlled condition was applied by deforming the periodic box on the  $xy$  plane implementing Lees-Edwards boundary conditions [36] at a fixed volume and temperature (canonical NVT ensembles) and a constant shearing rate  $\dot{\gamma} = 10^{-4}$  ps $^{-1}$  up to a 20% strain.

## III. DEFORMATION PATTERNS: DIFFUSE VS LOCALIZED

We performed a series of shear tests on the quenched samples with the resulting load curves  $\sigma_{xy}$  against applied shear strain  $\gamma$  reported in Fig. 2(a). In all the simulated glasses, the stress rises monotonically toward a peak stress followed by a sheer reduction in strength as the loading continues. We note that the  $\text{Co}_5\text{Cr}_2\text{Fe}_{40}\text{Mn}_{27}\text{Ni}_{26}$  metallic glass exhibits a very pronounced and abrupt stress drop that is typically accompanied by *sharp* localized (but system-spanning) strain

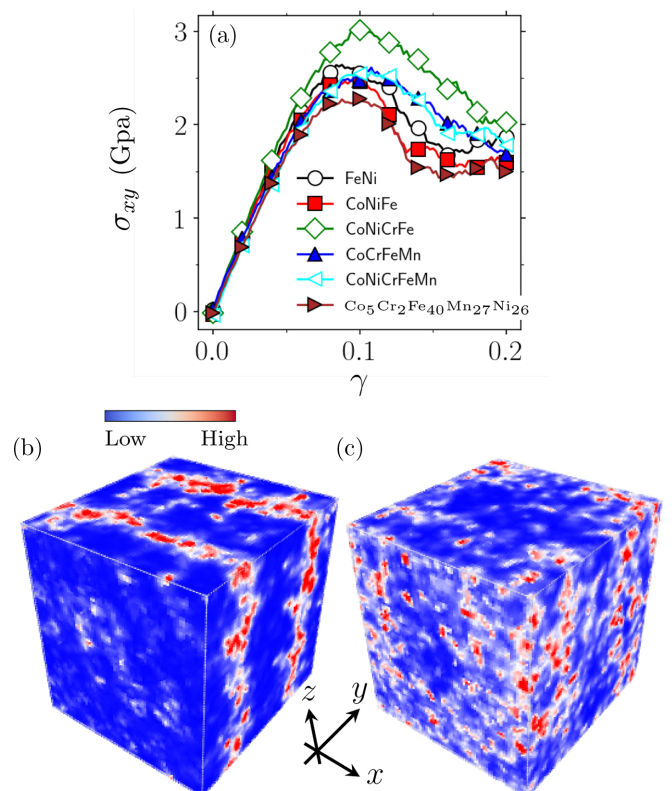


FIG. 2. (a) Macroscopic stress  $\sigma_{xy}$  plotted against applied (shear) strain  $\gamma$  corresponding to several metallic glasses. Local (interpolated) squared nonaffine displacements maps associated with the (b)  $\text{Co}_5\text{Cr}_2\text{Fe}_{40}\text{Mn}_{27}\text{Ni}_{26}$  and (c) CoNiCrFe glasses at  $\gamma = 0.2$ . Here  $x$ ,  $y$ , and  $z$  denote flow, gradient, and vorticity directions, respectively.

features as illustrated in Fig. 2(b) at  $\gamma = 0.2$ . The blue and red colors in the deformation maps indicate regions with low and high squared nonaffine displacements (see Sec. IV). The CoNiCrFe alloy almost shows identical stress features with an exception that the postyielding behavior occurs in a smoother manner. These metals should be referred to as good glasses with a high susceptibility to localize deformation. The other compositions, the so-called bad glasses, seem to indicate a shallower stress decay that is associated with rather *diffuse* deformation patterns across the medium, as in Fig. 2(c).

In this case, the glass responds in a homogeneous manner by nucleating multiple mesoscale deforming regions that are distributed almost uniformly across the medium. Similar maps at additional strains  $\gamma = 0.07, 0.13, 0.16$  (corresponding to prefailure and postfailure regimes) are illustrated in Figs. 11 and 12 in the Appendix. Prefailure strains (i.e.,  $\gamma = 0.07$ ) seem to indicate similar (diffuse) patterns for both good (Fig. 11) and bad (Fig. 12) glasses, which otherwise exhibit distinct deformation features at and beyond failure ( $\gamma \geq 0.1$ ).

Intuitively, the blue matrix in the deformation maps serve as fertile spots for the nucleation of SROs whereas the red (hot) regions should be structurally rich in terms of STZ clusters. Yet, there is an evolving fraction of icosahedral arrangements that tend to coexist with STZs within the hot spots. We argue that the observed coexistence indeed contributes to structural heterogeneities associated to the sheared

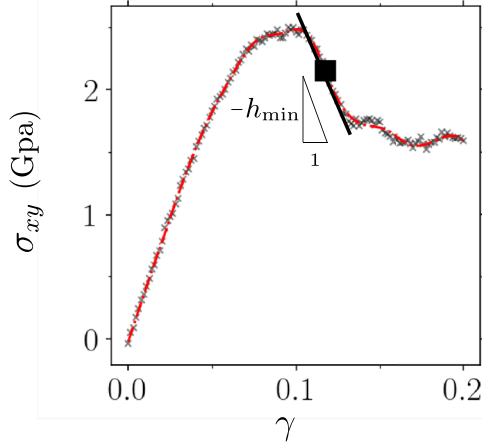


FIG. 3. Illustration of the softening modulus  $h_{\min}$ . The (black) crosses indicate the stress data  $\sigma_{xy}$  as a function of the applied (shear) strain  $\gamma$ . The dash-dotted (red) curve denotes a nonlinear fit based on (cubic) smoothing splines. The square symbol indicates the strain corresponding to the minimal slope past the stress peak  $\sigma_p$  as illustrated by the straight line

glass and, effectively, controls its quality (i.e., goodness versus badness) upon failure.

#### IV. STRUCTURE-DYNAMICS-PROPERTY RELATION

We now turn to relevant structural and dynamical metrics and search for possible connections with glass properties. As a starting point, dynamics of individual atoms is quantified by  $D_{\min}^2$  as a measure of deviations from affine trajectories of atoms imposed by an external (homogeneous) shear [3]. We fit a linear model based on the reference positions  $\vec{r}$  at zero strain, i.e.,  $\vec{R}(\vec{r}) = \mathbf{F}\vec{r} + \vec{F}_0$ , to the current atomic positions  $\vec{r}$  associated with  $N_b$  atoms within a given volume [37] by minimizing the squared loss function  $\mathcal{L}(\mathbf{F}, \vec{F}_0) = \sum_{i=1}^{N_b} |\vec{r}_i - \vec{R}(\vec{r}_i)|^2$  to obtain  $\{\hat{\mathbf{F}}, \hat{\vec{F}}_0\} = \text{argmin} \mathcal{L}(\mathbf{F}, \vec{F}_0)$ . Here the second-ranked deformation tensor  $\mathbf{F}$  and the (rigid) translation vector  $\vec{F}_0$  correspond to an affine transformation. The squared non-affine displacements for atom  $i$  is defined as  $D_i^2 = |\vec{r}_i - \hat{\vec{r}}_i|^2$  with  $\hat{\vec{r}}_i$  being the predicted position  $\vec{R}(\vec{r}_i) = \hat{\mathbf{F}}\vec{r}_i + \hat{\vec{F}}_0$  due to affine deformations.

Next, we performed a Voronoi analysis using OVITO [38] to locate atoms with an icosahedral symmetry—that is, Voronoi cells with exactly 12 polyhedral faces with 5 edges each. To obtain the associated (number) density,  $\rho_i^{\text{ico}} = 1/V_i^{\text{ico}}$ , we repeated the Voronoi analysis by including *exclusively* atom  $i$ 's with icosahedral symmetries within the periodic box (and excluding the other atoms). This gives another set of Voronoi cells (not to be confused with the original Voronoi set) with volume  $V_i^{\text{ico}}$  of atom index  $i$ . The mean number density of icosahedral clusters is denoted by  $\langle \rho^{\text{ico}} \rangle$ . We further employed the other structure characterization methods based on the radial distribution function  $g(r)$  and strain localization width  $w_{\text{sb}}$ . Finally, the glass quality, as a mechanical property, was gauged based on the softening modulus

$$h_{\min} = \partial_\gamma \sigma_{xy} |_{\min} \quad (1)$$

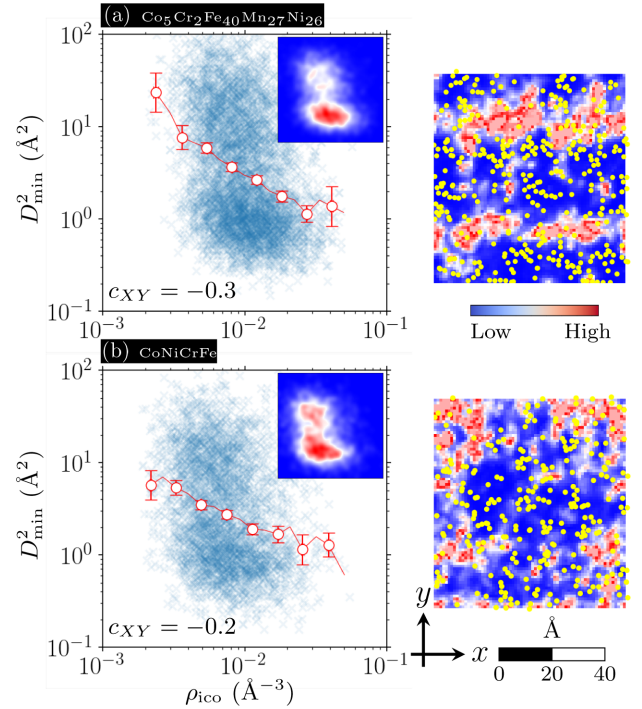


FIG. 4. Linking local icosahedral ordering with  $D_{\min}^2$  in the (a)  $\text{Co}_5\text{Cr}_2\text{Fe}_{40}\text{Mn}_{27}\text{Ni}_{26}$  and (b)  $\text{CoNiCrFe}$  glasses at  $\gamma = 0.2$ . The left panels display scatter plots of  $D_{\min}^2$  and icosahedra density  $\rho_{\text{ico}}$  with the (red) symbols denoting binning averaged data (in log space). The corresponding  $D_{\min}^2$  maps are shown on the right with the blue and red colors indicating regions with low and high nonaffine displacements. The (yellow) dots denote atoms with full icosahedral order. The insets are the same as the scatter plots but interpolated on a regular grid. Error bars denote two standard errors.

denoting the rate of stress decay associated with the maximum instability state upon failure (see Fig. 3). In the following subsections, we probe intercorrelations between the above metrics and outline commonalities and differences based on our “good-versus-bad” theme.

#### A. Structural & Dynamical Descriptors

The color maps in Fig. 4 overlay atoms with the full icosahedral order (yellow disks) on the two-dimensional (interpolated)  $D_{\min}^2$  field associated with the  $\text{Co}_5\text{Cr}_2\text{Fe}_{40}\text{Mn}_{27}\text{Ni}_{26}$  (top) and  $\text{CoNiCrFe}$  (bottom) metallic glasses. It is very clear on both maps that (red) rearranging regions significantly lack local structural ordering as opposed to the (blue) rigid matrix. As a metric to quantify this observation, a cross correlation analysis was carried out between the squared non-affine displacements of the yellow discs and the associated (number) density  $\rho_{\text{ico}}$ . The scatter data of  $D_{\min}^2$  and  $\rho_{\text{ico}}$  are shown in Figs. 4(a) and 4(b) along with the binning-averaged data (in the logarithmic space). The observed trend indicates significant (anti-)correlations between the logarithm of the two observables  $X = \log_{10} D_{\min}^2$  and  $Y = \log_{10} \rho_{\text{ico}}$  with the (linear) correlation coefficient  $c_{XY} \simeq -0.3, -0.2$  associated with  $\text{Co}_5\text{Cr}_2\text{Fe}_{40}\text{Mn}_{27}\text{Ni}_{26}$  and  $\text{CoNiCrFe}$ , respectively. Here  $c_{XY} = \langle \hat{X}_i \hat{Y}_i \rangle$  where  $\langle \cdot \rangle_i$  denotes averaging over the atom index  $i$  and  $\hat{X}$  indicates the fluctuating part (with the mean value

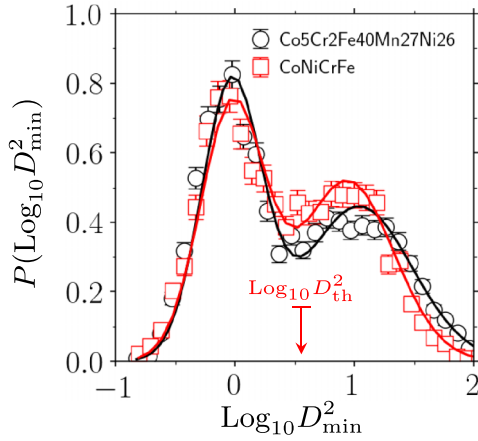


FIG. 5.  $D_{\min}^2$  probability distribution function of atoms with the full icosahedral order corresponding to the  $\text{Co}_5\text{Cr}_2\text{Fe}_{40}\text{Mn}_{27}\text{Ni}_{26}$  and  $\text{CoNiCrFe}$  glasses at  $\gamma = 0.2$ . The solid curves indicate results of the Gaussian mixture model.  $D_{\text{th}}^2$  indicated by the arrow separates the two populations. The error bars denote standard errors.

subtracted) normalized by the standard deviation associated with each variable.

Stronger anticorrelations associated with the “good” glass imply an infrequent occurrence of the structural ordering within the deforming bands potentially indicative of a strain-softening mechanism. The “bad” glass, by contrast, favors a spontaneous formation of (relatively) denser icosahedral clusters inside shear zones with partial strengthening effects that may account for the shallow stress decay associated with its bulk response. Variations in the relative fraction of ordered clusters is also manifested in the corresponding  $D_{\min}^2$  probability distribution function. As shown in Fig. 5, both glasses exhibit a clear bimodal behavior with the first higher and second lower peaks denoting the population of icosahedral clusters forming outside and within shear zones, respectively. We show the same probability distributions in Fig. 13 in the Appendix but at multiple applied strains, which tend to develop a modest hump at low strains. Results of the Gaussian mixture model associated with the (bad)  $\text{CoNiCrFe}$  glass (the red squares) indicates a relatively higher contribution of the ordered icosahedral phase to the plastic flow in comparison with the (good)  $\text{Co}_5\text{Cr}_2\text{Fe}_{40}\text{Mn}_{27}\text{Ni}_{26}$  metallic glass (the black circles). This observation is also in line with the outcomes of our correlation analysis.

Our analysis suggests that the interplay between the shear zones dynamics and nucleation of ordered icosahedral clusters might indeed control the extent of shear banding instability in metallic glasses. In this framework, we probed the evolution of such correlations with the applied strain as well as their variation with glass compositions. Figure 6(a) illustrates that the degree of (anti)correlations between  $D_{\min}^2$  and  $\rho_{\text{ico}}$  grows monotonically with strain by the time it saturates at  $\gamma \simeq 0.2$  but also reveals meaningful variations with the glass quality. As shown in Fig. 6(b), the latter, quantified by  $h_{\min}$ , strongly correlates with the ultimate correlation value where better glasses (with lower  $h_{\min}$ ) correspond, on average, to a lower  $c_{XY}^{\infty}$ .

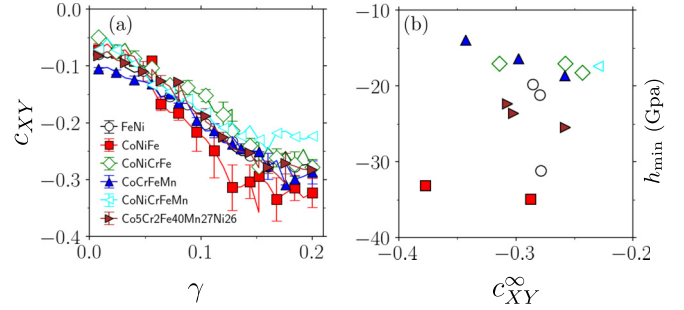


FIG. 6. (a) Evolution of the correlation coefficient  $c_{XY}$  with applied strain  $\gamma$  in several metallic glasses. (b) Scatter plot of the softening modulus  $h_{\min}$  and (terminal) correlation value  $c_{XY}^{\infty}$  associated with different glasses. Each symbol on the right denotes a set of different realizations corresponding to a specific glass composition.

We further note that both short-range ordering and non-affine displacements evolve with the applied strain as in Fig. 14 in the Appendix. The (mean) number density of icosahedral clusters  $\langle \rho^{\text{ico}} \rangle$  in Fig. 14(a) tend to go down with increasing  $\gamma$ . As shown in Fig. 14(b), this “amorphization” is accompanied by an overall growth in the squared nonaffine displacements  $\langle D_{\min}^2 \rangle$  averaged over different atoms. While the initial ordering (at  $\gamma = 0$ ) indicate a clear dependence on the chemical composition, the associated reduction (by the time of its saturation at larger strains) is fairly constant for every alloy. Such (initial) structural differences between alloys seem to influence (to some degree) the deformation dynamics (i.e.,  $\langle D_{\min}^2 \rangle$ ) and shear-banding instability (as quantified by  $h_{\min}$ ) within the failure regime. Interrelations between the above metrics are quantified in the color map and scatter plots of Figs. 10 and 17 (in the Appendix).

Another structural metric we probed is the radial distribution function, which should allow for discerning local structural differences leading to the observation of fundamentally different dynamics. As for the bad glasses, we speculate that the favorable icosahedra formation within plastic zones may have a signature on local density fluctuations around highly rearranging atoms. We make an appropriate conditioning on  $g(r)$  by including center atoms  $i = 1 \dots N_{\alpha}$  with  $D_{\min}^2 > D_{\text{th}}^2$ , i.e.,

$$g_{\alpha}(r) = \frac{1}{4\pi r^2 \Delta r N_{\alpha} \bar{\rho}} \sum_{i=1}^{N_{\alpha}} \sum_{j=1}^N \delta(r - r_{ij}), \quad (2)$$

with the mean number density of the system  $\bar{\rho}$ , discretization distance  $\Delta r$ , Kronecker delta  $\delta(\cdot)$ , and pairwise distance  $r_{ij}$  of atoms  $i$  and  $j$ . Here the chosen threshold  $D_{\text{th}}^2$  separates the two  $D_{\min}^2$  populations as in Fig. 5. Figure 7 plots the conditioned  $g(r)$  associated with the  $\text{Co}_5\text{Cr}_2\text{Fe}_{40}\text{Mn}_{27}\text{Ni}_{26}$  and  $\text{CoNiCrFe}$  glasses as well as the difference between that of the latter and the former. We note that, despite significant differences in icosahedral ordering and dynamic properties, the two metals have almost identical pair distribution functions. Nevertheless, the first few characteristic peaks in  $g(r)$  corresponding to  $\text{CoNiCrFe}$  are slightly higher than those of  $\text{Co}_5\text{Cr}_2\text{Fe}_{40}\text{Mn}_{27}\text{Ni}_{26}$  (see the green diamonds). This may indicate a relatively stronger presence of short-range ordering within shear spots of the former glass, which were shown to

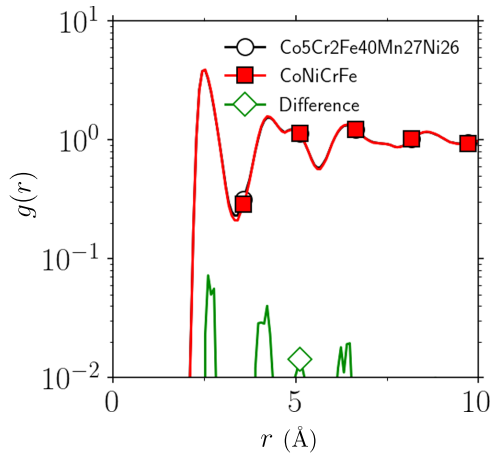


FIG. 7. Pair distribution function  $g_\alpha(r)$  of the  $\text{Co}_5\text{Cr}_2\text{Fe}_{40}\text{Mn}_{27}\text{Ni}_{26}$  and  $\text{CoNiCrFe}$  glasses at  $\gamma = 0.2$  conditioned based on  $D_{\min}^2 > D_{\text{th}}^2$  (see Fig. 5) associated with center atoms.

be richer (relative to the latter metal) in terms of the density of icosahedral clusters. We further notice slight variations of unconditioned  $g(r)$  and the height of its first peak (denoted by  $g_p^0$  at zero strain) with the composition in Fig. 15 in the Appendix. This may indicate differences in terms of the initial ordering and potential correlations with the mean density of icosahedral clusters ( $\rho_{\text{ico}}$ ). However,  $g(r)$  did not exhibit any significant evolution with applied strain.

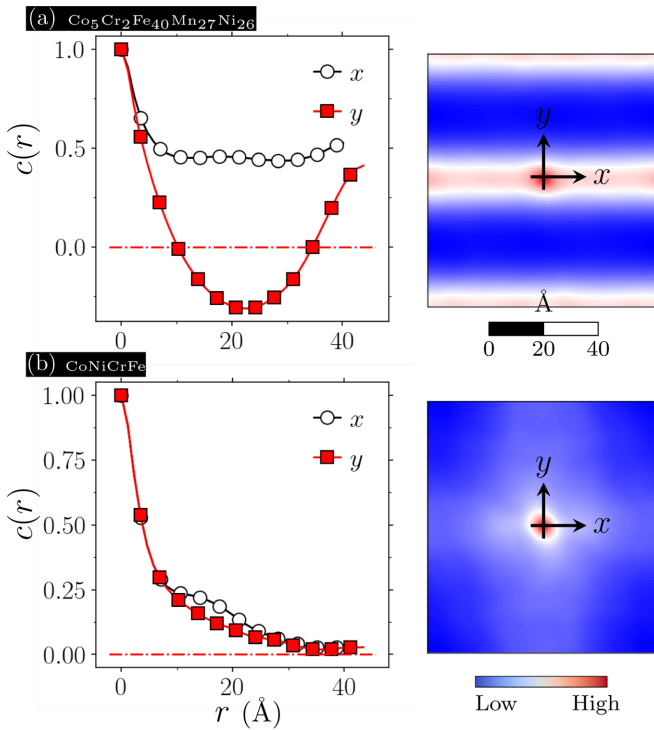


FIG. 8.  $D_{\min}^2$  correlations corresponding to the (a)  $\text{Co}_5\text{Cr}_2\text{Fe}_{40}\text{Mn}_{27}\text{Ni}_{26}$  and (b)  $\text{CoNiCrFe}$  glasses at  $\gamma = 0.2$ . The correlation function  $c(r)$  is plotted along the flow direction  $x$  and gradient direction  $y$ . The correlation maps  $c(x, y, z = 0)$  are shown on the right. The flat (dash-dotted) line indicate zero correlations.

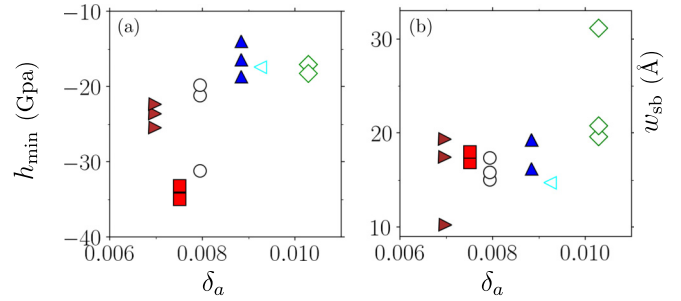


FIG. 9. Scatter plot of (a) softening modulus  $h_{\min}$  and (b) shear band width  $w_{\text{sb}}$  plotted against the size mismatch parameter  $\delta_a$  corresponding to the  $\text{FeNi}$  (o),  $\text{CoNiFe}$  (■),  $\text{CoNiCrFe}$  (◇),  $\text{CoCrFeMn}$  (▲),  $\text{CoNiCrFeMn}$  (◆),  $\text{Co}_5\text{Cr}_2\text{Fe}_{40}\text{Mn}_{27}\text{Ni}_{26}$  (▴) metallic glasses.

## B. Shear Band Characterization

Naturally, topological features associated with the shear band nucleation in metallic glasses should have a strong bearing on the dynamics of stress near the failure point. Along these lines, we made measurements of shear band widths  $w_{\text{sb}}$  as a useful metric to quantify the degree of strain localization and sought for potential correlations with the softening modulus  $h_{\min}$ . In the context of an ideal plastic behavior (with  $h_{\min} \simeq 0$ ), flow is accompanied by the “percolation” of multiple small-scale shear transformations that tend to spread homogeneously all across the system. In this case, one may assume that the shear band width approaches the system size, i.e.,  $w_{\text{sb}} \simeq L$ . On the other hand, brittle fracture is typically associated with the propagation of extremely localized but

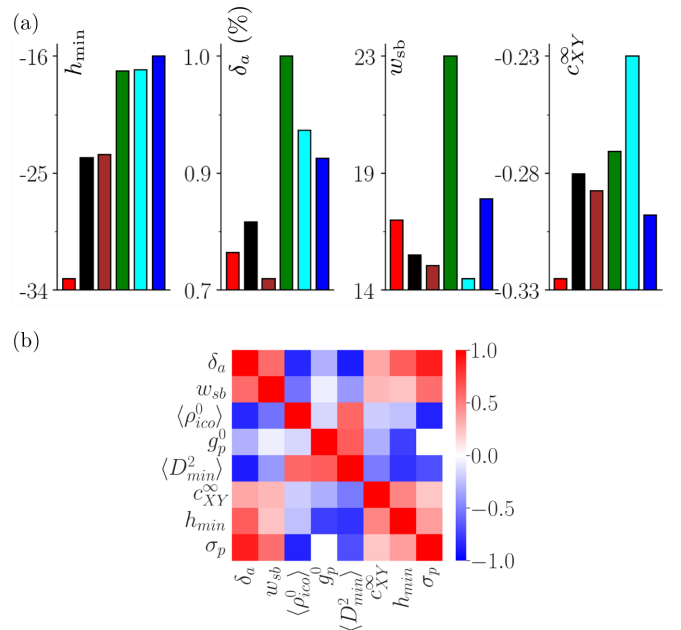


FIG. 10. (a) Softening modulus  $h_{\min}$ , Misfit parameter  $\delta_a$ , shear band width  $w_{\text{sb}}$ , and structure-dynamics correlations  $c_{XY}^\infty$  corresponding to the  $\text{FeNi}$  (■),  $\text{CoNiFe}$  (■),  $\text{CoNiCrFe}$  (■),  $\text{CoCrFeMn}$  (■),  $\text{CoNiCrFeMn}$  (■),  $\text{Co}_5\text{Cr}_2\text{Fe}_{40}\text{Mn}_{27}\text{Ni}_{26}$  (■) metallic glasses. (b) Correlation matrix associated with the metrics shown in Fig. 17. The color bar indicates correlation coefficients.

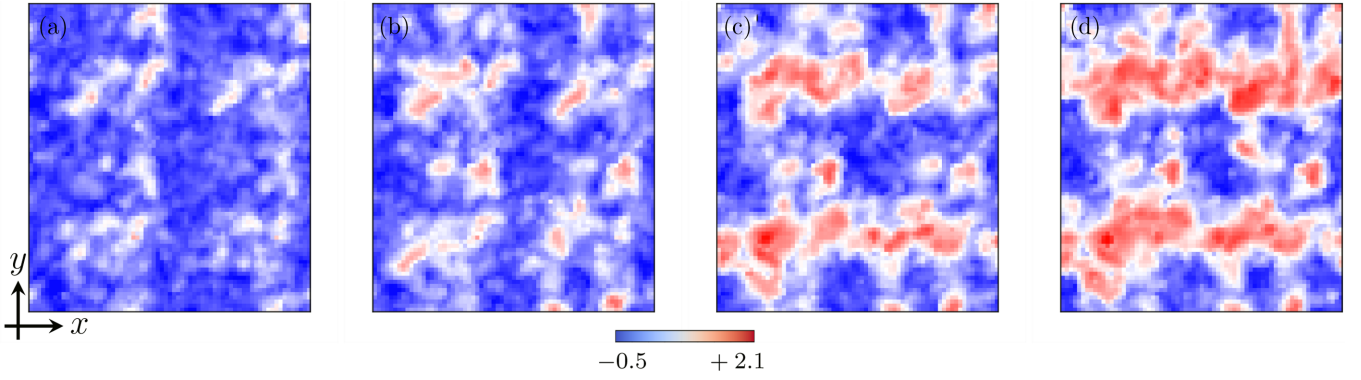


FIG. 11.  $D_{\min}^2$  maps on a logarithmic scale and associated evolution with applied strain at (a)  $\gamma = 0.07$  (b)  $\gamma = 0.10$  (c)  $\gamma = 0.13$  (d)  $\gamma = 0.16$  in sheared  $\text{Co}_5\text{Cr}_2\text{Fe}_{40}\text{Mn}_{27}\text{Ni}_{26}$ . Here  $x$  and  $y$  denote flow and gradient directions, respectively.

system-spanning crack-like deformation features [39] often leading to singular stress curve (with  $h_{\min} \rightarrow -\infty$  in the theoretical limit) [8]. The following aims to explore such an intimate relationship between  $w_{sb}$  and  $h_{\min}$  in the context of metallic glasses.

We performed an autocorrelation analysis on local  $D_{\min}^2$  fields to extract relevant micro-structural lengths. We start by interpolating the squared nonaffine atomic displacements on a fine cubic grid to obtain the autocorrelation function

$$c(\vec{r}) = \langle \hat{D}_{\min}^2(\vec{r}' + \vec{r}) \cdot \hat{D}_{\min}^2(\vec{r}') \rangle, \quad (3)$$

with  $\hat{D}_{\min}^2 \doteq (D_{\min}^2 - \langle D_{\min}^2 \rangle) / \text{var}^{1/2}(D_{\min}^2)$ . Figures 8(a) and 8(b) displays the correlation results corresponding to  $\text{Co}_5\text{Cr}_2\text{Fe}_{40}\text{Mn}_{27}\text{Ni}_{26}$  and  $\text{CoNiCrFe}$  glasses at  $\gamma = 0.2$ . In Fig. 8(a),  $c(r)$  associated with the former alloy shows an early decay regime along the flow direction  $x$  before entering a plateau regime at a bigger  $r$  due to the shear band formation that spans across the system [see the map of Fig. 4(a)].

Along the gradient direction  $y$ , however,  $c(r)$  exhibits a nonmonotonic behavior; it crosses zero at  $r \simeq 10$  Å and reaches a minimum at a larger length implying the presence of strong anticorrelations. The former length should give a reasonable width estimate for the nucleated bands, in visual agreements with the  $D_{\min}^2$  map of Fig. 4(a). Negative correlations may suggest a “coexistence” between intensely deforming plastic zones and the surrounding solid-like matrix with negligible shear deformation. The autocorrelation func-

tion becomes positive at  $r > 35$  Å owing to the spontaneous formation of two shearing bands, which are roughly apart by the indicated distance. The  $\text{CoNiCrFe}$  glass, on the other hand, shows monotonic slowly-decaying correlations in both  $x$  and  $y$  directions hitting the noise floor at  $r \simeq 40$  Å, which is roughly half the physical system size. The picture is fairly consistent with the spatial structure of plastic zones with a fairly homogeneous distribution of nonaffine deformations across the bulk, as in Fig. 4(b).

Figure 9 plots the  $w_{sb}$  and  $h_{\min}$  estimates for different glasses against the corresponding atomic size mismatch parameter  $\delta_a = \sqrt{\text{var}(a_i)} / \langle a_i \rangle$ . The latter is defined as the normalized standard deviation associated with radius  $a_i$  of atom  $i = 1 \dots N$ . In the context of high-entropy alloys,  $\delta_a$  is believed to strongly control the degree of local lattice distortions [40]. We generalize this concept to glassy alloys where the size mismatch parameter may be thought as a structural proxy controlling the degree of quenched disorder. Here  $\delta_a$  varies between 1 – 2%. The scatter plot of the softening modulus  $h_{\min}$  and size mismatch  $\delta_a$  in Fig. 9(a) indicates a positive correlation between the two observables. Likewise, the shear band width  $w_{sb}$  in Fig. 9(b) seem to be statistically related (apart from the outliers). Our data also suggest that the glass goodness, featured by  $h_{\min}$ , tends to correlate with the localization degree measured by  $w_{sb}$  with a correlation coefficient close to 0.2 (see Figs. 10 and 17 [in the Appendix]). We further probed the local misfit parameter  $\delta_a^{\text{loc}}$  and its spatial

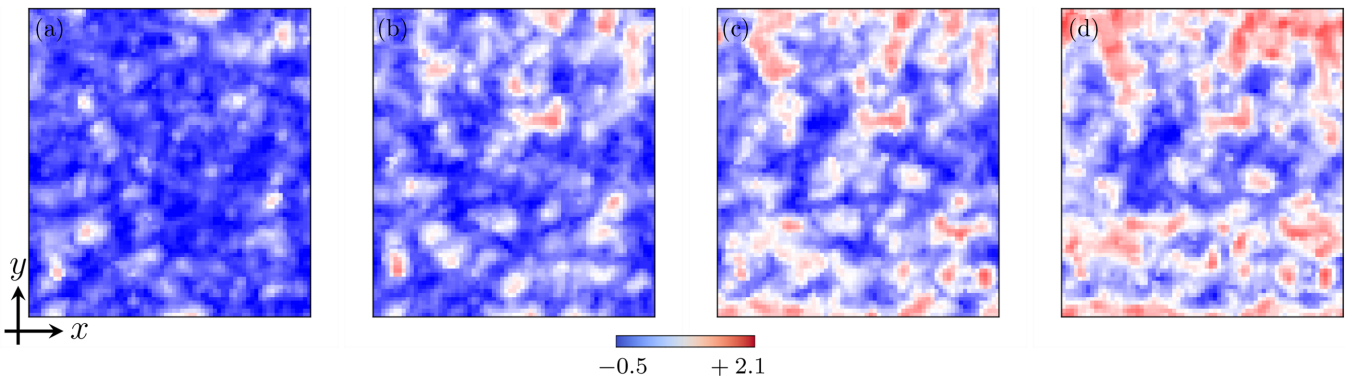


FIG. 12. The same as Fig. 11 but in a sheared  $\text{CoNiCrFe}$ .

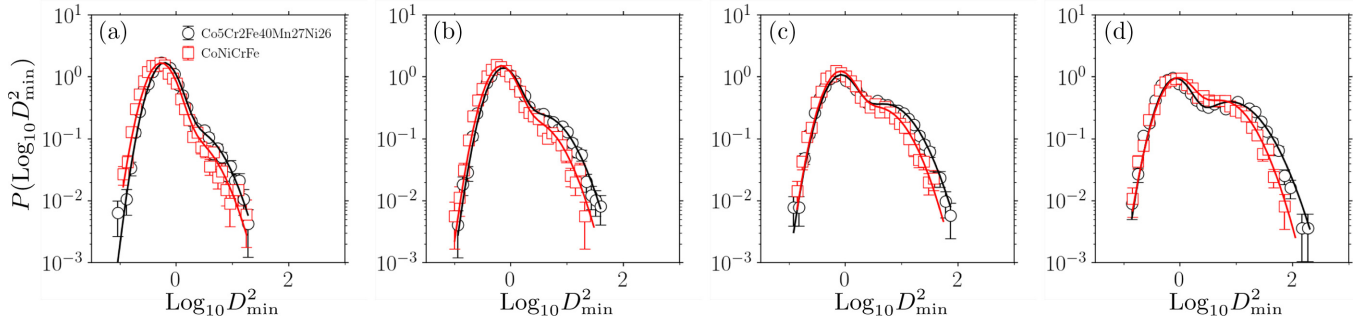


FIG. 13.  $D_{\min}^2$  probability distribution function of atoms with the full icosahedral order corresponding to the  $\text{Co}_5\text{Cr}_2\text{Fe}_{40}\text{Mn}_{27}\text{Ni}_{26}$  and  $\text{CoNiCrFe}$  glasses at (a)  $\gamma = 0.07$ , (b)  $\gamma = 0.10$ , (c)  $\gamma = 0.13$ , and (d)  $\gamma = 0.16$ . The solid curves indicate results of the Gaussian mixture model. The error bars denote standard errors.

distribution in Fig. 16 in the Appendix, which is indicative of local compositional variations within shear bands. In Fig. 16 (Left panel), the probability distribution functions  $P(\delta_a^{\text{loc}})$  and associated conditioning based on the presence and absence of SRO's do not suggest statistically significant differences. The spatial map in Fig. 16 (Right panel), however, may indicate an overall tendency for icosahedral clusters to form within high  $\delta_a^{\text{loc}}$  regions.

## V. DISCUSSION

Our atomistic simulations of sheared metallic glasses with several principal components have led to the observation of different strain patterns, ranging from a homogeneous plastic-like flow to shear band dominated localized deformation, in agreement with previous numerical and experimental studies. We have found a direct relevance of underlying microstructure on the atomic-scale dynamics, which strongly correlates with the observed deformation features as well as the bulk mechanical response upon failure. Our Voronoi-based analysis demonstrates the prevalence of the short-range order based on an icosahedral symmetry attributed to the local inter-atomic topology. Atoms with the observed symmetry are found to be less prone to undergo intense shear transformations. This has been validated by observing pronounced anticorrelation features between (atomic-scale) nonaffine displacements and

density of icosahedral clusters. Our correlation analysis is similar in essence to the methodology used in [41,42] connecting local structure and dynamics in several glass forming metals. This provides a useful metric to measure structural (in)homogeneities within shear bands, which also strongly couple to the glass ability to (de)localize strain. The extent of bimodality in the nonaffine displacement distributions is another signature of inherent heterogeneities in a glassy metal that may limit shear strain localization. To our knowledge, this bimodal behavior had not been previously reported in the literature. Based on the radial distribution function data, sheared samples with uniform deformation patterns tend to have (relatively) abundant solid-like structures within flowing regions, which may be also understood in terms of the heterogeneity notion. The latter was further quantified topologically through the (effective) band width measurements, which show meaningful variations with the rate of stress decay (as a bulk mechanical property) as well as intrinsic heterogeneities associated with the constituent elements' radii.

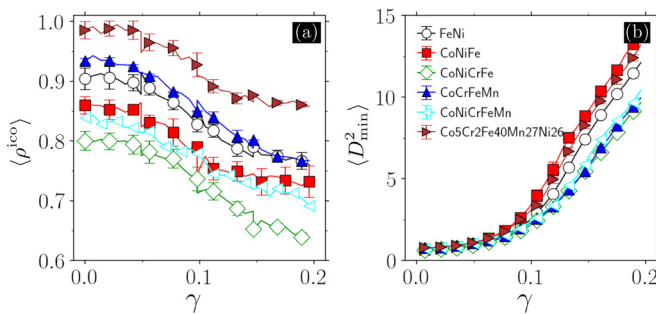


FIG. 14. (a) Mean (number) density of atoms with icosahedral symmetries  $\langle \rho^{\text{ico}} \rangle$ . (b) Mean squared nonaffine displacements  $\langle D_{\min}^2 \rangle$  plotted against applied strain  $\gamma$  corresponding to different metallic glasses. The error bars indicate standard errors.

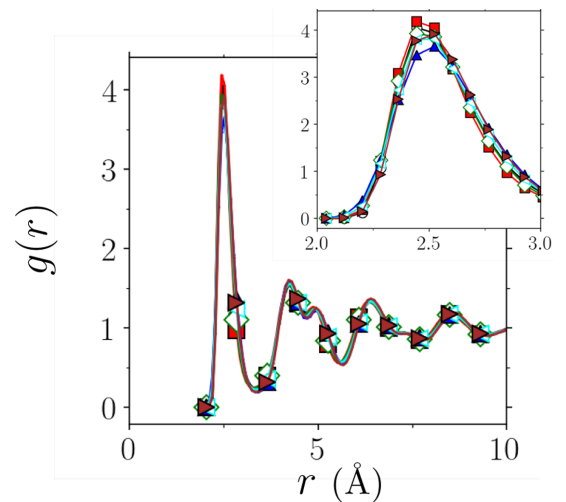


FIG. 15. Initial pair distribution function  $g(r)$  at  $\gamma = 0.0$  (unstrained samples) corresponding to the  $\text{FeNi}$  (o),  $\text{CoNiFe}$  (■),  $\text{CoNiCrFe}$  (◇),  $\text{CoCrFeMn}$  (▲),  $\text{CoNiCrFeMn}$  (◊),  $\text{Co}_5\text{Cr}_2\text{Fe}_{40}\text{Mn}_{27}\text{Ni}_{26}$  (▾) metallic glasses. The inset is the same as the main plot but with a magnified view around the first peak.



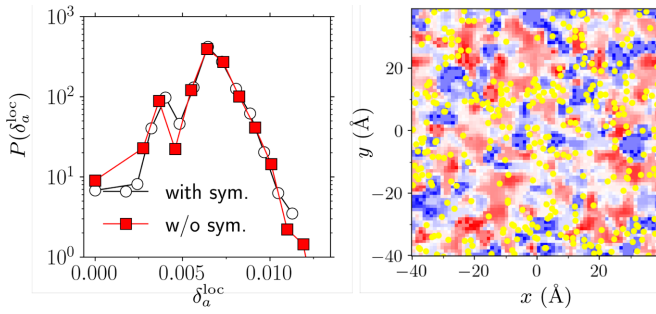


FIG. 16. Linking local icosahedral ordering with local misfit parameter  $\delta_a^{\text{loc}}$  in  $\text{Co}_5\text{Cr}_2\text{Fe}_{40}\text{Mn}_{27}\text{Ni}_{26}$  glass at  $\gamma = 0.2$ . The left panel displays probability distributions  $P(\delta_a^{\text{loc}})$  including atoms with the icosahedral symmetry (red squares) and otherwise (black circles). The corresponding  $\delta_a^{\text{loc}}$  map is shown on the right with the blue and red colors indicating regions with low and high local misfit. The (yellow) dots denote atoms with full icosahedral order.

Figure 10 provides a summary of key compositional/structural/mechanical metrics probed in this study. The bar charts sort the element compositions for each index based on the ascending order in the softening modulus  $h_{\text{min}}$  (with the lowest  $h_{\text{min}}$  marking the best glass). Based on the observed trends in the data,  $h_{\text{min}}$  qualitatively correlates with  $\delta_a$  but also, with the shear band width  $w_{\text{sb}}$  and structure-dynamic correlations  $c_{XY}^{\infty}$ . One may, however, infer stronger (positive) correlations between the studied order parameters within the scatter data as in Fig. 17 (in the Appendix) owing to the fact that the bar charts illustrate *mean* quantities associated with  $h_{\text{min}}$ ,  $w_{\text{sb}}$ , and  $c_{XY}^{\infty}$  over different realizations. Our data indicate that good glasses—with lowest  $h_{\text{min}}$ ,  $w_{\text{sb}}$ , and  $c_{XY}^{\infty}$ —statistically correlate with low misfits, opposite to the commonly-observed trend that the glass forming ability (in the thermodynamics sense) tends to improve with increasing  $\delta_a$ . In other words, a glass that shears well is not a good glass former.

A larger set of metrics including initial icosahedra density  $\langle \rho_{\text{ico}}^0 \rangle$ , the first peak in the pair correlation function  $g_p^0$ , mean squared nonaffine displacements  $\langle D_{\text{min}}^2 \rangle$ , and peak stress  $\sigma_p$  (see Fig. 3) together with corresponding correlation coefficients are displayed in the correlation matrix of Fig. 10 and the scatter matrix plot in Fig. 17 in the Appendix.  $\langle \rho_{\text{ico}}^0 \rangle$  shows strong anticorrelations with  $\delta_a$  as it is anticipated that an increase in the latter leads to a stronger glass forming ability and, therefore, a suppression of SROs marked by the former. Similar trends may be observed between  $\langle D_{\text{min}}^2 \rangle$  and  $\delta_a$ . Positive correlations between  $\langle \rho_{\text{ico}}^0 \rangle$  and  $\langle D_{\text{min}}^2 \rangle$  sound rather counterintuitive as a dense population of icosahedra clusters would naively mean a less propensity for shear rearrangements. Our scatter data also indicate that an increase in  $\delta_a$  statistically leads to a higher peak stress  $\sigma_p$  (or ultimate strength) in studied glasses. Another counterintuitive observation is the negative dependence of  $\sigma_p$  on  $\langle \rho_{\text{ico}}^0 \rangle$ , quite contrary to the speculation that icosahedral symmetries often improve local yield properties. Negative correlations between  $\langle D_{\text{min}}^2 \rangle$  and  $\sigma_p$  is meaningful as less propensity to shear rearrangements should imply a stronger glass. Anticorrelations between  $h_{\text{min}}$  and  $\langle D_{\text{min}}^2 \rangle$  should imply that a sharp yielding transition is accompanied by intense shear rearrangements.

$h_{\text{min}}$  negatively correlates with  $g_p^0$  meaning that initial ordering tends to increase the transition sharpness.

Our local misfit  $\delta_a^{\text{loc}}$  analysis within shear bands did not indicate distinguishable compositional fluctuations compared to the surrounding matrix. This may suggest that the formation of SROs might be largely independent of the “color” of constituent atoms. Recent experimental observations, however, report on distinct elemental redistributions inside shear bands that contrast the compositionally-homogeneous structure elsewhere in the medium [43,44]. In-depth numerical investigations of such composition-based variations and their relevance in terms of micro-structural tailoring could be an interesting topic as a future study.

The above observations highlight the significance of chemical compositions and demand for a more systematic search strategy over a much broader composition space to design desired glasses. It is, therefore, essential to seek for a more descriptive and comprehensive set of relevant structural/physical/mechanical features and probe potential correlations with specific material properties, a training task amenable to materials informatics [14].

The microstructural heterogeneity highlighted in our study must have a strong bearing on local elasticity and associated fluctuations in space [19]. The latter is a key element in STZ-based mesoscopic models, which typically make no direct reference to atomic-scale disorder but instead take into consideration elastic heterogeneity as a main (often phenomenological) model ingredient. These mesoscale treatments, however, largely ignore true microstructural origins associated with elastic inhomogeneity above some certain scales, which in turn impair predictive capacities of coarse-grained approaches. In this framework, a direct structural characterization of metallic glasses (via simulations and/or experiments) seems necessary in that local atomic configurations can provide insights on the nature of elastic heterogeneity and its multiscale notion in glassy materials. These efforts should lead to significant improvements in existing coarse-grained models without compromising the true underlying physics.

We note that SRO-induced inhomogeneities and their relevance on the degree of strain localization may not be specific to multicomponent metallic glasses but could also be pertinent in their mono-atomic counterparts or even in the context of other amorphous solids. Despite having an extremely low glass forming ability [6], single-element metallic glasses may be still synthesized under very high quench rates [45] in the laboratory or based on other experimental techniques [46]. On the other hand, model single-component metallic glasses were shown to contain SROs at atomic scales [47,48] and, therefore, the proposed mechanisms involving SRO and its interplay with STZs could potentially govern their shear response. However, the universality of such a picture has yet to be explored experimentally and numerically.

## VI. CONCLUSIONS

In summary, we have identified relevant structural features associated with differing degrees of strain localization observed in mechanically deforming model metallic glasses. We have based our approach on finding meaningful links between

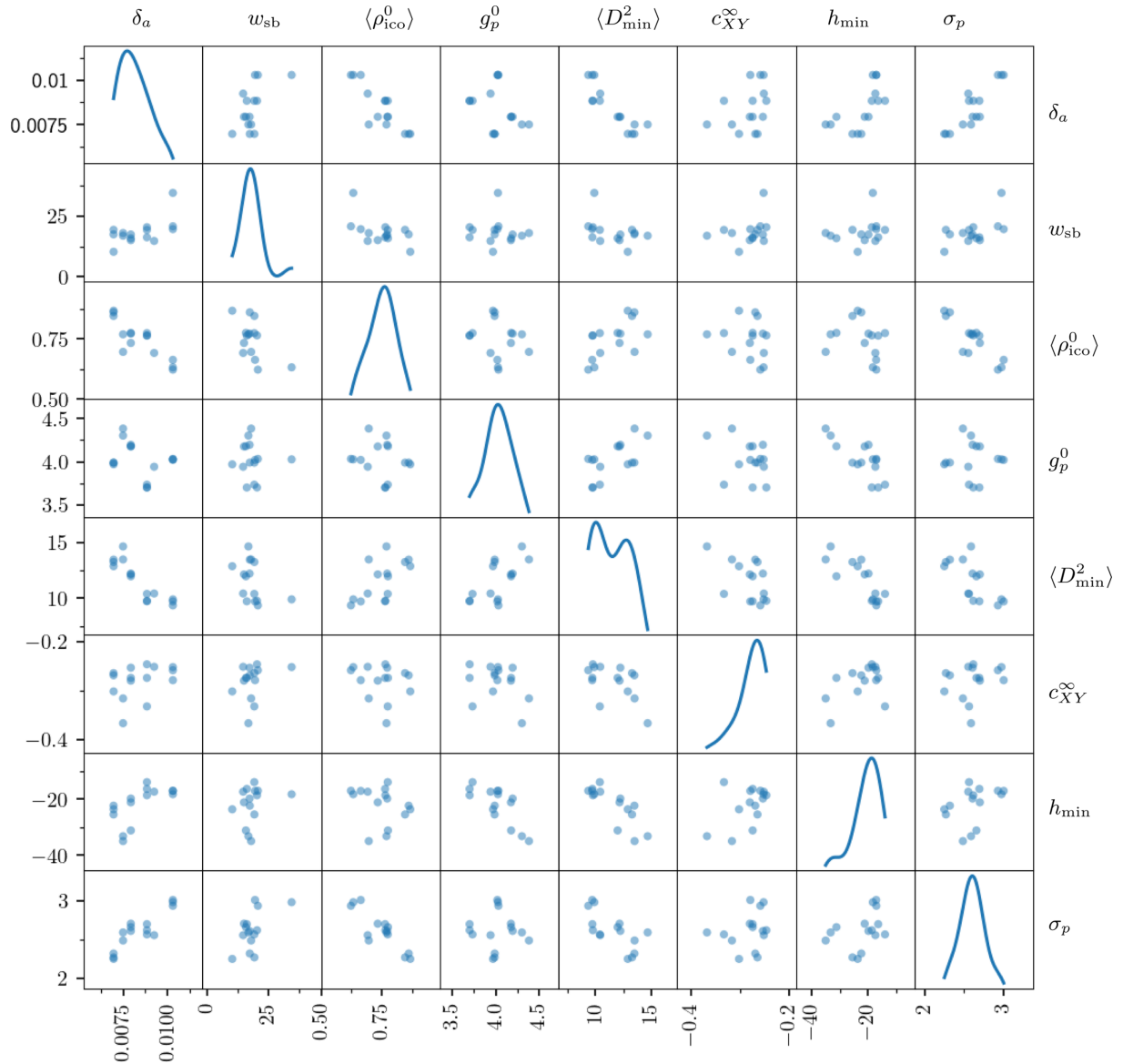


FIG. 17. Scatter matrix plot including misfit parameter  $\delta_a$ , shear band width  $w_{sb}$ , initial (mean) icosahedra density  $\langle \rho_{ico}^0 \rangle$ , the first peak of the pair correlation function  $g_p^0$ , mean squared nonaffine displacements  $\langle D_{min}^2 \rangle$ , structure-dynamics correlations  $c_{XY}^\infty$ , softening modulus  $h_{min}$ , and peak stress  $\sigma_p$ . The diagonal panels show corresponding histograms.

the microstructure and atomic-scale dynamics in response to an external (shear) stress. In particular, we established that (i) structural heterogeneity controls the glass quality described based on the degree of strain localization and sharpness of plastic yielding transition, (ii) the lack of SRO's within shearing bands with low susceptibility against localized rearrangements enhance band formation in good glasses, and (iii) an abundance of short range ordering within shear zones in bad glasses increases structural inhomogeneity and local hardening and, therefore, their ability to delocalize strain. Our results have important implications in terms of microstructural tuning to optimize specific glass properties.

#### ACKNOWLEDGMENTS

This research was funded by the European Union Horizon 2020 research and innovation program under Grant Agreement No. 857470 and from the European Regional

Development Fund via Foundation for Polish Science International Research Agenda PLUS Program Grant No. MAB PLUS/2018/8.

#### APPENDIX: CORRELATION ANALYSIS

In this Appendix, we will provide additional plots of our correlation analyzes relevant to the six different metallic glasses discussed in the main text.

Squared nonaffine displacements  $D_{min}^2$  maps and associated evolution with applied strain  $\gamma$  in sheared  $\text{Co}_5\text{Cr}_2\text{Fe}_{40}\text{Mn}_{27}\text{Ni}_{26}$  and  $\text{CoNiCrFe}$  are displayed in Figs. 11 and 12, respectively. Figure 13 plots associated  $D_{min}^2$  probability distributions conditioned based on atoms with icosahedral symmetries. In Fig. 14, the number density of atoms with an icosahedral symmetry and  $\langle D_{min}^2 \rangle$  (averaged over different atoms) are plotted against applied strain  $\gamma$  in different alloys. Figure 15 shows the radial distribution function  $g(r)$

corresponding to unstrained glasses at  $\gamma = 0.0$ . Figure 16 links local icosahedral ordering with *local* misfit parameter  $\delta_a^{\text{loc}}$  in  $\text{Co}_5\text{Cr}_2\text{Fe}_{40}\text{Mn}_{27}\text{Ni}_{26}$  glass at  $\gamma = 0.2$ . The analysis involved partitioning of the entire simulation box into subvolumes using a cubic grid of size  $4.0 \text{ \AA}$ , which is close to twice the radius associated with the first peak of  $g(r)$  in Fig. 15. The local misfit parameter  $\delta_a^{\text{loc}}$  was subsequently determined based

on the scaled standard deviation of atoms' radii within each cube (see the map in Fig. 16). Figure 17 shows scatter matrix plots of misfit parameter  $\delta_a$ , shear band width  $w_{\text{sb}}$ , mean icosahedra density  $\langle \rho_{\text{ico}}^0 \rangle$ , the first peak in the pair correlation function  $g_p^0$ , mean squared nonaffine displacements  $\langle D_{\text{min}}^2 \rangle$ , structure-dynamics correlations  $c_{XY}^\infty$ , softening modulus  $h_{\text{min}}$ , and stress peak  $\sigma_p$ .

- 
- [1] R. Maaß and J. F. Löffler, Shear-band dynamics in metallic glasses, *Adv. Funct. Mater.* **25**, 2353 (2015).
- [2] A. Argon and H. Kuo, Plastic flow in a disordered bubble raft (an analog of a metallic glass), *Mater. Sci. Eng.* **39**, 101 (1979).
- [3] M. L. Falk and J. S. Langer, Dynamics of viscoplastic deformation in amorphous solids, *Phys. Rev. E* **57**, 7192 (1998).
- [4] M. L. Falk and J. S. Langer, Deformation and failure of amorphous, solidlike materials, *Annu. Rev. Condens. Matter Phys.* **2**, 353 (2011).
- [5] K. Karimi and J.-L. Barrat, Correlation and shear bands in a plastically deformed granular medium, *Sci. Rep.* **8**, 4021 (2018).
- [6] O. Senkov and D. Miracle, Effect of the atomic size distribution on glass forming ability of amorphous metallic alloys, *Mater. Res. Bull.* **36**, 2183 (2001).
- [7] Z. Li, S. Zhao, R. O. Ritchie, and M. A. Meyers, Mechanical properties of high-entropy alloys with emphasis on face-centered cubic alloys, *Prog. Mater. Sci.* **102**, 296 (2019).
- [8] M. Ozawa, L. Berthier, G. Biroli, A. Rosso, and G. Tarjus, Random critical point separates brittle and ductile yielding transitions in amorphous materials, *Proc. Natl. Acad. Sci. USA* **115**, 6656 (2018).
- [9] D. V. Denisov, K. A. Lőrincz, W. J. Wright, T. C. Hufnagel, A. Nawano, X. Gu, J. T. Uhl, K. A. Dahmen, and P. Schall, Universal slip dynamics in metallic glasses and granular matter—linking frictional weakening with inertial effects, *Sci. Rep.* **7**, 43376 (2017).
- [10] K. Karimi, E. E. Ferrero, and J.-L. Barrat, Inertia and universality of avalanche statistics: The case of slowly deformed amorphous solids, *Phys. Rev. E* **95**, 013003 (2017).
- [11] K. Karimi, D. Amitrano, and J. Weiss, From plastic flow to brittle fracture: Role of microscopic friction in amorphous solids, *Phys. Rev. E* **100**, 012908 (2019).
- [12] H. Ding and K. Yao, High entropy  $\text{Ti}_{20}\text{Zr}_{20}\text{Cu}_{20}\text{Ni}_{20}\text{Be}_{20}$  bulk metallic glass, *J. Non-Cryst. Solids* **364**, 9 (2013).
- [13] W. Li, P. Liu, and P. K. Liaw, Microstructures and properties of high-entropy alloy films and coatings: A review, *Mater. Res. Lett.* **6**, 199 (2018).
- [14] K. Frydrych, K. Karimi, M. Pecelerowicz, R. Alvarez, F. J. Dominguez-Gutiérrez, F. Rovaris, and S. Papanikolaou, Materials informatics for mechanical deformation: A review of applications and challenges, *Materials* **14**, 5764 (2021).
- [15] Y. Lu, Z. Zhang, X. Lu, Z. Qin, J. Shen, Y. Huang, and P. K. Liaw, Cooling-rate induced softening in a colloidal glass, *Sci. Rep.* **7**, 16882 (2017).
- [16] C. A. Schuh, T. C. Hufnagel, and U. Ramamurty, Mechanical behavior of amorphous alloys, *Acta Mater.* **55**, 4067 (2007).
- [17] D. Şopu, A. Stukowski, M. Stoica, and S. Scudino, Atomic-Level Processes of Shear Band Nucleation in Metallic Glasses, *Phys. Rev. Lett.* **119**, 195503 (2017).
- [18] M. Hassani, A. E. Lagogianni, and F. Varnik, Probing the Degree of Heterogeneity within a Shear Band of a Model Glass, *Phys. Rev. Lett.* **123**, 195502 (2019).
- [19] N. Wang, J. Ding, F. Yan, M. Asta, R. O. Ritchie, and L. Li, Spatial correlation of elastic heterogeneity tunes the deformation behavior of metallic glasses, *npj Comput. Mater.* **4**, 1 (2018).
- [20] Y. Fan, T. Iwashita, and T. Egami, Evolution of elastic heterogeneity during aging in metallic glasses, *Phys. Rev. E* **89**, 062313 (2014).
- [21] E. Ma and J. Ding, Tailoring structural inhomogeneities in metallic glasses to enable tensile ductility at room temperature, *Mater. Today* **19**, 568 (2016).
- [22] K. Wang, T. Fujita, Y. Zeng, N. Nishiyama, A. Inoue, and M. Chen, Micromechanisms of serrated flow in a  $\text{Ni}_{50}\text{Pd}_{30}\text{P}_{20}$  bulk metallic glass with a large compression plasticity, *Acta Mater.* **56**, 2834 (2008).
- [23] J. Das, M. B. Tang, K. B. Kim, R. Theissmann, F. Baier, W. H. Wang, and J. Eckert, “Work-Hardenable” Ductile Bulk Metallic Glass, *Phys. Rev. Lett.* **94**, 205501 (2005).
- [24] S.-W. Lee, M.-Y. Huh, E. Fleury, and J.-C. Lee, Crystallization-induced plasticity of Cu–Zr containing bulk amorphous alloys, *Acta Mater.* **54**, 349 (2006).
- [25] J. Ding, Y.-Q. Cheng, and E. Ma, Full icosahedra dominate local order in  $\text{Cu}_{64}\text{Zr}_{34}$  metallic glass and supercooled liquid, *Acta Mater.* **69**, 343 (2014).
- [26] J. Ding, Y. Cheng, and E. Ma, Correlating local structure with inhomogeneous elastic deformation in a metallic glass, *Appl. Phys. Lett.* **101**, 121917 (2012).
- [27] J. Ding, S. Patinet, M. L. Falk, Y. Cheng, and E. Ma, Soft spots and their structural signature in a metallic glass, *Proc. Natl. Acad. Sci. USA* **111**, 14052 (2014).
- [28] Y. Shi and M. L. Falk, Strain Localization and Percolation of Stable Structure in Amorphous Solids, *Phys. Rev. Lett.* **95**, 095502 (2005).
- [29] Y. Shi and M. L. Falk, Atomic-scale simulations of strain localization in three-dimensional model amorphous solids, *Phys. Rev. B* **73**, 214201 (2006).
- [30] Y. Shi and M. L. Falk, Stress-induced structural transformation and shear banding during simulated nanoindentation of a metallic glass, *Acta Mater.* **55**, 4317 (2007).
- [31] T. C. Hufnagel, C. A. Schuh, and M. L. Falk, Deformation of metallic glasses: Recent developments in theory, simulations, and experiments, *Acta Mater.* **109**, 375 (2016).
- [32] C. Alcock, O. Kubaschewski, and P. Spencer, *Materials Thermochimistry* (Pergamon Press, London, 1993).

- [33] A. Inoue, Stabilization of metallic supercooled liquid and bulk amorphous alloys, *Acta Mater.* **48**, 279 (2000).
- [34] S. Plimpton, Fast parallel algorithms for short-range molecular dynamics, *J. Comput. Phys.* **117**, 1 (1995).
- [35] W.-M. Choi, Y. H. Jo, S. S. Sohn, S. Lee, and B.-J. Lee, Understanding the physical metallurgy of the CoCrFeMnNi high-entropy alloy: An atomistic simulation study, *npj Comput. Mater.* **4**, 1 (2018).
- [36] A. Lees and S. Edwards, The computer study of transport processes under extreme conditions, *J. Phys. C* **5**, 1921 (1972).
- [37] The  $D_{\min}^2$  analysis involves partitioning of the entire box into sub-volumes using a cubic grid of size  $r_c = 3.0 \text{ \AA}$ , which is close to twice the radius associated with the first peak of  $g(r)$ .
- [38] A. Stukowski, Visualization and analysis of atomistic simulation data with ovito—the open visualization tool, *Modell. Simul. Mater. Sci. Eng.* **18**, 015012 (2010).
- [39] P. Cao, K. A. Dahmen, A. Kushima, W. J. Wright, H. S. Park, M. P. Short, and S. Yip, Nanomechanics of slip avalanches in amorphous plasticity, *J. Mech. Phys. Solids* **114**, 158 (2018).
- [40] Y. Shang, J. Brechtel, C. Psitidda, and P. K. Liaw, Mechanical behavior of high-entropy alloys: A review, [arXiv:2102.09055](https://arxiv.org/abs/2102.09055).
- [41] Z. Fan, J. Ding, and E. Ma, Machine learning bridges local static structure with multiple properties in metallic glasses, *Mater. Today* **40**, 48 (2020).
- [42] Q. Wang and A. Jain, A transferable machine-learning framework linking interstice distribution and plastic heterogeneity in metallic glasses, *Nat. Commun.* **10**, 5537 (2019).
- [43] S. Balachandran, J. Orava, M. Köhler, A. J. Breen, I. Kaban, D. Raabe, and M. Herbig, Elemental re-distribution inside shear bands revealed by correlative atom-probe tomography and electron microscopy in a deformed metallic glass, *Scr. Mater.* **168**, 14 (2019).
- [44] C. Liu, Z. Cai, X. Xia, V. Roddatis, R. Yuan, J. Zuo, and R. Maaß, Shear-band structure and chemistry in a zr-based metallic glass probed with nano-beam x-ray fluorescence and transmission electron microscopy, *Scr. Mater.* **169**, 23 (2019).
- [45] L. Zhong, J. Wang, H. Sheng, Z. Zhang, and S. X. Mao, Formation of monatomic metallic glasses through ultrafast liquid quenching, *Nature (London)* **512**, 177 (2014).
- [46] Q. An, S.-N. Luo, W. A. Goddard III, W. Han, B. Arman, and W. L. Johnson, Synthesis of single-component metallic glasses by thermal spray of nanodroplets on amorphous substrates, *Appl. Phys. Lett.* **100**, 041909 (2012).
- [47] S. Becker, E. Devijver, R. Molinier, and N. Jakse, Glass-forming ability of elemental zirconium, *Phys. Rev. B* **102**, 104205 (2020).
- [48] S. Trady, A. Hasnaoui, M. Mazroui, and K. Saadouni, Local atomic structures of single-component metallic glasses, *Eur. Phys. J. B* **89**, 223 (2016).